VELOCITY MEASUREMENTS IN THE NEAR WAKE OF A HORIZONTAL AXIS WIND TURBINE

W. Haans, T. Sant, G.A.M. van Kuik and G.J.W. van Bussel
Delft University of Technology
Delft, The Netherlands

Abstract

Single film hot-film measurements in the near wake of a horizontal axis wind turbine are performed in the Delft University of Technology Open Jet Facility in order to capture the blade azimuth dependent velocity vectors. A novel approach to determine the average, blade azimuth dependent, velocity vector is proposed. It makes use of the asymmetric response of hot-films that have the film parallel to its probe. Contrary to the traditional approach in which the direction of velocity components cannot be determined and which poorly predicts relatively small velocity components, the proposed method yields velocity direction as part of the solution and consistently predicts relatively small velocity components. An uncertainty analysis is performed on the velocity magnitude and flow angle, quantifying the data quality. Furthermore, comparisons with previously published data on the same rotor, in the same wind tunnel are made. The comparisons increase confidence in the data and reveal the advantages of the proposed velocity determination method. Qualitatively, the velocity signals derived with the proposed approach are in agreement with expectations from a general vortex wake model, also the relatively small tangential and radial velocity components.

Nomenclature

A	speed calibration constant [-]
a	axial induction factor [-]
B	speed calibration constant [-]
c	airfoil chord [m]
c_T	thrust coefficient [-]
DUT	Delft University of Technology
E	hot-film voltage [V]
f	rotational frequency [s^{-1}]
$HAWT$	horizontal axis wind turbine
h	angular calibration constant [-]
k	angular calibration constant [-]
N	number of data points [-]
n	speed calibration constant [-]
OJF	Open Jet Facility
(r, θ, z)	cylindrical coordinate system
R_r	rotor root radius [m]
R_t	rotor tip radius [m]
$Re_{0.7R}$	chord Reynolds number at $0.7R_t$ [-]
s	standard deviation
T	axial force [N]
T_a	flow temperature [K]
T_f	hot-film temperature [K]
$Tu_{0.7R}$	turbulence intensity at $0.7R_t$ [-]
$U_{\lvert V\rvert}$	velocity magnitude random uncertainty [m/s]
U_α	flow angle random uncertainty [m/s]
(U_m, V_m, W_m)	velocity in Cartesian coordinate system (x_m, y_m, z_m) [m/s]
(U_p, V_p, W_p)	velocity in Cartesian coordinate system (x_p, y_p, z_p) [m/s]
(V_r, V_θ, V_z)	velocity in cylindrical coordinate system (r, θ, z) [m/s]
V_{eff}	effective velocity [m/s]
$W_{jet\text{-}exit}$	tunnel exit axial velocity [m/s]
(x_m, y_m, z_m)	global cartesian coordinate system, attached to model support
(x_p, y_p, z_p)	local cartesian coordinate system, attached to hot-film
α	flow angle [°]
θ	blade pitch angle [°]
θ_b	blade azimuth angle [°]
θ_{tip}	tip pitch angle [°]
θ^*	azimuth-domain excluding region of highly non-axisymmetrical axial induction factor [°]
Δ	difference
λ	tip speed ratio [-]
ν	kinematic viscosity [m^2/s]
Ψ	yaw angle [°]
<X>	ensemble (phase-locked) average of X
$\overline{X}$	time average of X

1 Introduction

Strong similarities between the vortical wake behind the rotor of a Horizontal Axis Wind Turbine (HAWT) and that of a helicopter can be observed. An analogy between forward helicopter flight and a HAWT operating in yawed flow conditions can be found as both result in a skewed wake. Zero forward helicopter movement corresponds to a HAWT operating in axial flow conditions.

Due to the complex, unsteady aerodynamics associated with especially yawed flow conditions, both physical understanding and

modelling are challenging and demand sustained efforts, as acknowledged by recent wind turbine rotor aerodynamics reviews (Ref. 1, 2). Measurements in controlled environments, hence wind tunnels instead of outdoor fields, are demanded. An excellent overview of both experimental and numerical research in the wake of HAWT's in axial flow conditions is given in Ref. 3.

A distinction can be made between the near wake and the far wake part. In the near wake, the area up to about one rotor diameter downstream, the properties of the rotor can be identified. Currently, the focus is on the three-dimensional velocities in the near wake of a HAWT. The experimental techniques applied to capture near wake unsteady velocities include hot-wire anemometry (Ref. 4-8) and particle image velocimetry (PIV) (Ref. 9, 10). Whereas hot-wire anemometry has the disadvantage that measurements are taken at discrete points instead of a plane as for PIV, hot-film anemometry is capable of determining the three-dimensional velocity vector.

The experiments cited in Ref. 6-8 are done with an X-probe type hot-wire. The direction of the velocity components is derived explicitly and much attention is given to turbulence quantities and repeatability of the data. The open jet wind tunnel diameter is of equal size as the two-bladed rotor diameter, hence blockage effects render the near wake measurements to only qualitatively represent a wind turbine, not quantitatively. Furthermore, yawed flow conditions are not considered.

Besides the near wake velocity measurements on the Delft University of Technology (DUT) model rotor (Ref. 4, 5), performance measurements and experiments on tip vortices (Ref. 11, 12) are carried out as well, both in axial flow conditions and in yaw. A measurement analysis tool is also developed (Ref. 13). Hence an extensive experimental database is available for this rotor. The near wake velocity measurements are carried out with a single wire hot-wire. The data reduction technique applied does not yield directions of the velocity components in the rotor plane; they need to be estimated instead. Furthermore, small velocity components are not determined consistently.

Current experiments on the DUT rotor model aim at determining all three components of the near wake velocities. Both axial and yawed flow conditions are considered. This publication focuses on axial flow conditions, as is this the baseline case. A further aim is to physically interpret the observed velocity signals.

This paper first discusses the experiments in the near wake. Thereafter, data reduction is presented, both the hot-wire calibration and the velocity determinations. The traditional approach, used previously on the DUT rotor data, and a novel, proposed technique are presented. Next, the resulting velocity signals are discussed and finally concluding remarks are made.

2 Experiments

2.1 Experimental Setup A two-bladed rotor model is placed in the Open Jet Facility (OJF) of the DUT in order to perform the near wake hot-film measurements. For a schematic of the setup, see Figure 1. The main characteristics of the OJF are a jet diameter of 2.24 m, a maximum attainable wind speed $W_{jet\text{-}exit,max}$ of 14.5 m/s and a turbulence level of 1.2±0.2% at

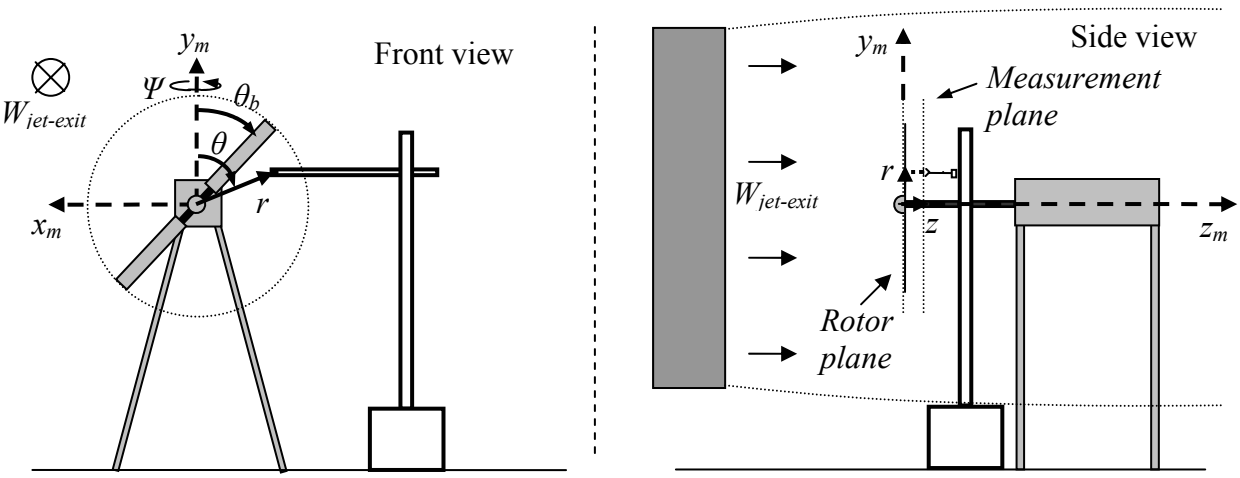

Figure 1. Schematic of the experimental setup, displaying the rotor model, the traversing rig and the wind tunnel exit. The global Cartesian coordinate system *(x_m, y_m, z_m)* is attached to the non-rotating model support, as is the global cylindrical coordinate system *(r, θ, z)*. θ_b is the blade azimuth angle, Ψ is the yaw angle, with y_m the yaw axis .

$W_{jet\text{-}exit}$ = 5.5 m/s, the speed at which the measurements are taken.
The readings from three inter-connected Pitot-static tubes, mounted in the jet exit plane, together with ambient pressure and jet temperature recordings, are used to derive $W_{jet\text{-}exit}$. The OJF is not equipped with a separate flow return channel; the tunnel hall is used for recirculation instead.
In Table 1, the geometric properties of the rotor model are described. The model offers the possibility to alter the blade pitch angle by modifying the tip pitch angle θ_{tip}. The rotor plane of the rotor model is located 1 m downstream of the jet exit plane, with the hub positioned at the jet center. The distance from the rotor plane to the downstream tunnel wall is 11 m or 18.4 rotor tip radii R_t. Axial force T, the force normal to the rotor plane, is recorded by means of strain gauges on the rotor shaft.

Table 1 Rotor main geometric characteristics

Number of blades	2
Airfoil section	NACA0012
Rotor tip radius R_t	0.6 m
Blade root radius R_r	0.18 m
Chord c	0.08 m
Blade pitch angle θ	$\theta(r/R)=(6+\theta_{tip})-6.67r/R$, $0.3\leq r/R\leq 0.9$
	$\theta(r/R)=\theta_{tip}$, $0.9<r/R\leq 1$

The velocities in the near wake of the rotor model are recorded by means of hot-film constant temperature anemometry. A single-film hot-film probe is mounted on a traversing rig that makes an automated traverse through a plane parallel to the rotor plane. Two types of single film hot-films are used; one with the film normal to the probe (TSI 1201-20) and one with the film parallel to the probe (TSI 1211-20), see Figure 2. Except for the hot-film orientation, the two types of probes are similar. Table 2 summarizes their characteristics.

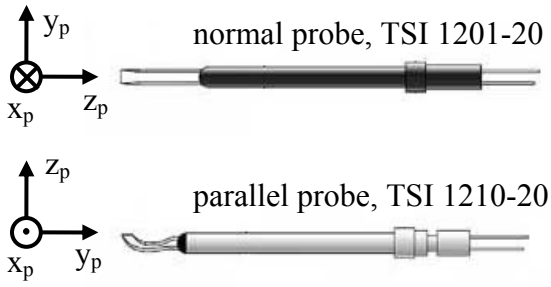

Figure 2. The normal and parallel types of single film hot-films used. Included is the local Cartesian coordinate system (x_p, y_p, z_p), attached to the hot-film. Note that the two coordinate systems differ.

The hot-film recordings are synchronized with the rotational frequency of the blades; every 2° blade azimuth angle θ_b a sample is taken. The hot-film sample rate is approximately 2.1 kHz, corresponding to a maximum frequency resolution of 1.0 kHz. The upper frequency limit for a cylindrical hot-film of about 75 kHz at 10 m/s (Ref. 14) will thus not limit the frequency response of these hot-film measurements.

Table 2 Hot film sensor main characteristics

Sensor material	Platinum film on fused-quartz substrate
Sensor diameter	50.8 μm
Sensor length	1.02 mm
Probe diameter	3.9 mm

2.2 Experimental Procedure A single flow condition is examined. The jet-exit plane wind speed is set to $W_{jet\text{-}exit}$ = 5.5 m/s. The blades rotate at f = 11.67 Hz. The ratio of rotational velocity versus undisturbed wind speed, named tip speed ratio λ, then is λ = 8, using

$$\lambda = \frac{2\pi f R_t}{W_{jet-exit}}. \qquad [1]$$

θ_{tip} is set to 2°. The yaw angle Ψ, being the angle between the normal to the rotor plane and the undisturbed velocity vector, is set to Ψ = 0°, 30° or 45°. The majority of the current discussion concerns axial flow, Ψ = 0°.
A fixed point on the blades, located at 0.7R_t, is selected where the chord Reynolds number $Re_{0.7R}$ and the turbulence intensity $Tu_{0.7R}$ are determined. For the determination of $Re_{0.7R}$ and $Tu_{0.7R}$, the velocity at the 0.7R_t-location is assumed to consist of the freestream and solid body rotation velocity contributions only. Hence, $Re_{0.7R}$ can be written as

$$\mathrm{Re}_{0.7R} = \frac{c\sqrt{W_{jet-exit}{}^2 + (2\pi f\, 0.7R)^2}}{\nu}, \qquad [2]$$

with c the airfoil chord and ν the kinematic viscosity. The present settings yield $Re_{0.7R}$ = $1.6\bullet 10^5$. $Tu_{0.7R}$ is determined using fluctuations in the axial velocity component only,

$$Tu_{0.7R} = \sqrt{\frac{\overline{w^2}}{\overline{W_{jet-exit}}^2 + (2\pi f\, 0.7R_t)^2}}. \qquad [3]$$

The disturbance term $\overline{w^2}$ is the orthogonal summation of two contributions; the variance of W, measured at a fixed position in the empty jet and the variance of a collection $\overline{W}$-values, gathered from rotational sampling of the 0.7R_t-point through a non-uniform flow field in the empty jet, see Figure 3. The non-uniform empty jet velocity profile is not axi-symmetrical,

61.3

resulting in the rotational sampling contribution to $Tu_{0.7R}$. The observed velocity dip in the empty jet is thought to be caused by the wake shed from the nacelle of the upstream fan. $Tu_{0.7R}$ is determined at 0.44 %.

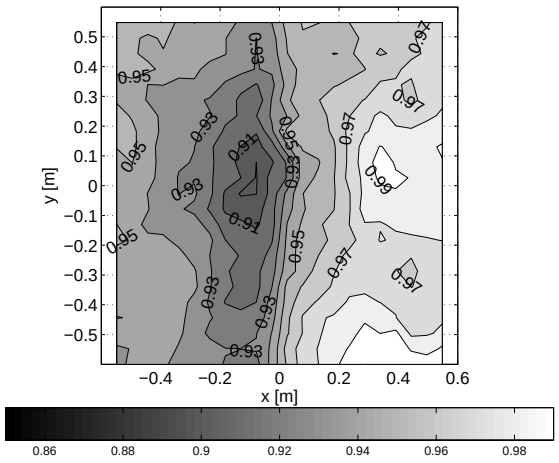

Figure 3. $\overline{W} / \overline{W_{jet-exit}}$ measured locally in the empty tunnel, at the rotor plane location, normalised with the maximum recorded value of $\overline{W} / \overline{W_{jet-exit}}$. ($x$, y) = (0, 0) corresponds to the hub center.

One plane 6 cm upstream of the rotor plane and three downstream planes, at 3.5 ($0.06R_t$), 6.0 ($0.1R_t$) and 9.0 cm ($0.15R_t$) from the rotor plane, are selected. The spatial resolution of the measurement points, expressed in cylindrical coordinates, is given by r = 0.24, 0.30,…, 0.60 m (r/R_t = 0.4, 0.5,…, 1), θ = 0°, 15°,…, 345°. For a given (r, θ, z) -location, a hot-film sample is taken every 2° blade azimuth angle θ_b, for a total of 54 blade cycles, resulting in 54 samples for each hot-film orientation at each (r, θ, z, θ_b)-point. Simultaneously, $W_{jet\text{-}exit}$ and f are recorded every cycle, each yielding 54 samples per (r, θ, z)-coordinate.

Hot-film recordings at multiple orientations are required to estimate the velocity magnitude and direction (Ref. 14). Since single film type probes are relatively inexpensive and calibration-friendly, compared to multiple film types, single film hot-films are used.

Six hot-film orientations are required for the data reduction technique proposed in §3.2. Due to the limited range of the traversing rig, half of the measurement plane is measured at the time.

A traverse takes about 30 minutes. Errors between intended and true measurement positions due to random drifts of the traversing mechanism accumulate and result into an offset when returning to the starting point upon completion of a measurement traverse. After each measurement traverse, the offset is determined and the starting point is reset.

A hot-film is sensitive to both magnitude and direction of the flow. Calibrations first determine the relationship between the hot-film output voltage and speed with the film normal to the flow (speed calibration) and then, for a given speed, the relationship between voltage and flow angles (angular calibration). Both speed and angular calibration are performed regularly to compensate for hot-film ageing

A measurement campaign solely dedicated to the determination of the axial force coefficient c_T is conducted (Ref. 12).

3 Data Reduction

Hot-films are sensitive to the direction of the flow. Coordinate system conventions thus need to be made, in order to perform hot-film calibrations and velocity determinations. A global Cartesian coordinate system (x_m, y_m, z_m), fixed to the rotor support structure, and a local cartesian coordinate system (x_p, y_p, z_p), attached to the hot-film, is used, see Figures 1 and 2, respectively.

3.1 Calibration A speed calibration is the first step in the calibration procedure of the hot-film probes. The hot-film voltage E is correlated to a known wind speed W_m with the hot-film normal to the flow ($W_m = W_p$) using the temperature corrected, averaged King's law (Ref. 14)

$$\overline{E}^2 = \left(\overline{T_f} - \overline{T_a}\right)\left(A + B\overline{W_p}^n\right), \qquad [4]$$

T_f and T_a are the preset hot-film and measured flow temperature, respectively. A, B and n are calibration constants, with A set to $\left[\overline{E}^2 / \left(\overline{T_f} - \overline{T_a}\right)\right]_{W=0}$. B and n are found by curve fitting the measurement data in the least-square sense. The contribution from the standard deviation terms generally is several orders of magnitude smaller than the averages and is therefore ignored. The flow total and static pressure, needed to determine W_p, are recorded by a single pitot-static tube, located in the vicinity of the hot-film.

The second calibration step, angular calibration, determines the sensitivity of the hot-film to the flow direction. Generally, the direction and magnitude of the flow velocity are unknown beforehand. The recorded E is related to the velocity magnitude when the flow would have been normal to the film, named V_{eff}, using equation [4]. V_{eff} is correlated to the instantaneous velocity components using (Ref. 13)

$$V_{eff}^2 = h^2 U_p^2 + k^2 V_p^2 + W_p^2, \qquad [5]$$

where h and k are angular calibration constants and U_p, V_p and W_p are the velocity components in a cartesian coordinate system, fixed to the hot-film probe, see Figure 2. To determine the angular calibration constants, the hot-film is subjected to a constant axial velocity whilst being rotated in a vertical plane parallel to the axial direction. The hot-film is oriented such that U_p, V_p or W_p equals zero. An example orientation, using the normal hot-film probe, is given in Figure 4. For this case, averaging of equation [5] yields

$$\overline{V_{eff}}^2 = k^2 \left|\overline{\vec{V}}\right|^2 \sin^2\alpha + \left|\overline{\vec{V}}\right|^2 \cos^2\alpha\,, \qquad [6]$$

when ignoring the small standard deviation contribution. From the recording at α = 0°, $|\overline{\vec{V}}|$ is known. The system of 19 equations, for α = -90°, -80°,…, 90°, is solved in the least squares sense for the unknown k^2.

Angular calibrations are performed at various $|\overline{\vec{V}}|$-values. The computed k^2's and h^2's only show a small variation with $|\overline{\vec{V}}|$; for both the normal and the parallel hot-film probe, $k^2 \approx 0.1$ and $h^2 \approx 1.2$. When varying $|\overline{\vec{V}}|$ from about 4 to 7 m/s, the maximum variations in k^2 and h^2 are 0.01 and 0.03, respectively. The angular calibration constants are therefore considered independent of the flow speed, thereby significantly simplifying the data-reduction.

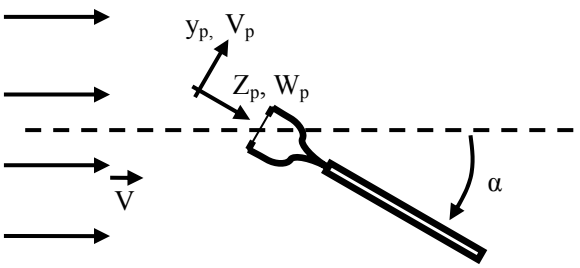

Figure 4. Schematic of the normal probe angular calibration orientation going with equation [6].

3.2 Velocity Determination The hot-film orientations needed to estimate the velocity magnitude and direction are recorded sequentially. As equation [5] holds instantaneously, it should be averaged to construct a system of equations with the hot-film in various orientations. Per (r, θ, z, θ_b)-point, the ensemble average of equation [5] is taken and the disturbance terms are neglected, yielding

$$\left\langle V_{eff} \right\rangle^2 = h^2 \left\langle U_p \right\rangle^2 + k^2 \left\langle V_p \right\rangle^2 + \left\langle W_p \right\rangle^2 . \qquad [7]$$

Generally, $\langle v_i^2 \rangle$ is several orders of magnitude smaller than $\langle V_i \rangle^2$, justifying the simplification to neglect the disturbance terms. A traditional and a newly proposed approach to determine $\langle \vec{V} \rangle(r, \theta, z, \theta_b)$ are discussed next. Both make use of equation [7].

The traditional method (Ref. 4, 5) needs three single film hot-film orientations. Two are taken with the normal probe, one with the parallel probe. Both normal probe orientations have the hot-film normal to the axial direction, one with the hot-film vertical, one wit the hot-film horizontal. The probe itself is parallel with the axial direction. The parallel probe has its hot-film oriented parallel to the axial direction, with the plane formed by the hot-film and the prongs oriented vertically. For each (r, θ, z, θ_b)-point, a system of three equations can be constructed using equation [7],

$$\begin{pmatrix} h_1^2 & k_1^2 & 1 \\ k_2^2 & h_2^2 & 1 \\ h_3^2 & 1 & k_3^2 \end{pmatrix} \begin{bmatrix} \langle U_m \rangle^2 \\ \langle V_m \rangle^2 \\ \langle W_m \rangle^2 \end{bmatrix} = \begin{bmatrix} \langle V_{eff,1} \rangle^2 \\ \langle V_{eff,2} \rangle^2 \\ \langle V_{eff,3} \rangle^2 \end{bmatrix}, \qquad [8]$$

and solved for $\langle U_m \rangle^2$, $\langle V_m \rangle^2$ *and* $\langle W_m \rangle^2$. Note that the cartesian coordinate system is no longer fixed to the hot-film probe (local), it is fixed to the non-rotating model support instead (global), see Figure 1.

The *direction* of the velocity components is not a part of the solution, since the *squared* velocity components are solved for. The generally large axial velocity component $\langle W_m \rangle$ of the rotor wake in axial flow conditions can be assumed to be in the downstream direction. The other two velocity components however are generally small, relative to the axial component, and their direction needs to be guessed.

Furthermore, because the $\langle U_m \rangle$ and $\langle V_m \rangle$ components are small and because of uncertainties in the data-reduction, the traditional data reduction at several (r, θ, z, θ_b)-points yield $\langle U_m \rangle^2 < 0$ and/or $\langle V_m \rangle^2 < 0$. This result is non-physical.

A new data reduction method for single film probes intends to overcome the problems of the traditional method; the absence of the velocity direction and the squared velocity values that are smaller than zero.

Basis for the proposed method is the asymmetric response of the parallel hot-film to the flow angle in the (y_p,z_p)-plane due to partial shielding of the hot-film by the prongs, see Figure 5. The asymmetry in the response to the W_p-component is independent of the value for $\langle V_{eff} \rangle_{\alpha=+90°}$, the three data-sets in Figure 5 align.

The asymmetry in the response of the parallel hot-film to the W_p-component can be used to determine the direction of the generally small global $\langle U_m \rangle$- and $\langle V_m \rangle$-components at a given

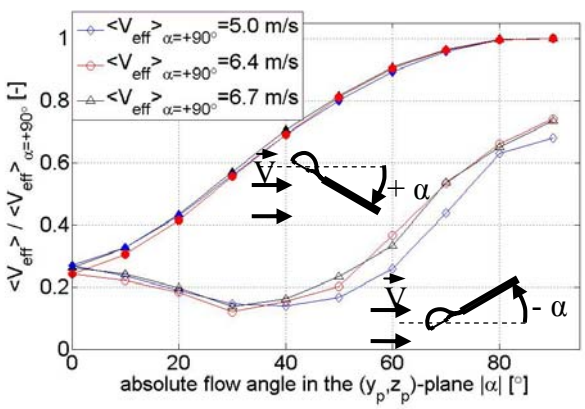

Figure 5. $\langle V_{eff}\rangle$, normalised with $\langle V_{eff}\rangle_{\alpha=+90°}$ versus α for the parallel probe. α defines the flow angle in the (y_p,z_p)-plane. The observed $\langle V_{eff}\rangle$-reading is asymmetrical with α: asymmetric W_p-response.

(r, θ, z, θ_b)-point.

The hot-film probe should therefore be oriented such that either $\langle U_m\rangle$ or $\langle V_m\rangle$ is aligned with the z_p-axis. Two orientations per global velocity component can be identified, see Figure 6 for the $\langle V_m\rangle$-component.

Hence, to determine the direction of both $\langle U_m\rangle$ and $\langle V_m\rangle$, a total of four parallel probe orientations are required. The direction of the axial velocity component $\langle W_m\rangle$ is not determined using this technique; it is assumed to be in the downstream direction instead because of the large values found for $|\langle W_m\rangle|$.

The magnitude of $\langle W_m\rangle$ is estimated with the traditional approach, using the system of equations [8]. The hot-film orientations are identical to those applied with the traditional approach.

The magnitude of $\langle U_m\rangle$ and $\langle V_m\rangle$ is estimated from the recordings of the pair of parallel probe orientations that is used to determine their respective directions. The procedure is given for $\langle V_m\rangle$, similar reasoning holds for $\langle U_m\rangle$ though. For the pair of orientations, see Figure 6, the one yielding the largest $\langle V_{eff}\rangle$-value for a given (r, θ, z, θ_b) -point is apparently oriented such that its prongs do not obstruct the flow.

The general relationship [7] can thus be used, written in global coordinates as

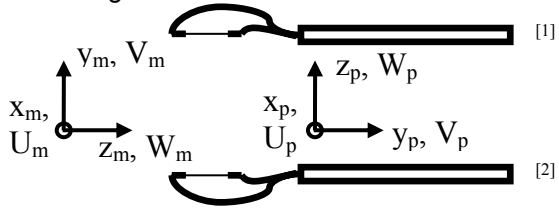

Figure 6. The two parallel probe orientations required to determine the direction of V_m.

$$\langle V_{eff,1}\rangle^2 = h^2\langle U_m\rangle^2 + \langle V_m\rangle^2 + k^2\langle W_m\rangle^2, \qquad [9]$$

with the suffix 1 denoting the non-blocking orientation. For the other orientation, a more general formulation is used,

$$\langle V_{eff,2}\rangle^2 = f\left(\langle U_m\rangle, \langle V_m\rangle, \langle W_m\rangle\right), \qquad [10]$$

with the suffix 2 indicating the blocking orientation.

The $\langle U_p\rangle$-component that is known from angular calibration to yield a symmetrical hot-film response aligns with the $\langle U_m\rangle$-component. The contribution from $\langle U_m\rangle$ to $\langle V_{eff}\rangle$ is therefore assumed to be the same for the two orientations and equal to $h^2\langle U_m\rangle^2$ from equation [9]. Equation [10] can be rewritten to

$$\langle V_{eff,2}\rangle^2 = g\left(\langle V_m\rangle, \langle W_m\rangle\right) + h^2\langle U_m\rangle^2. \qquad [11]$$

From angular calibration of the parallel probe in the (y_p,z_p)-plane, a correlation G between measured $\langle V_{eff}\rangle$-values and the absolute flow angle $|\alpha|=\arctan(|W_p/V_p|)$ exists,

$$\frac{\langle V_{eff,1}\rangle^2 - \langle V_{eff,2}\rangle^2}{\langle V_{eff,1}\rangle^2} = G\left(\arctan\left|\frac{\langle W_p\rangle}{\langle V_p\rangle}\right|\right), \qquad [12]$$

see Figure 7.

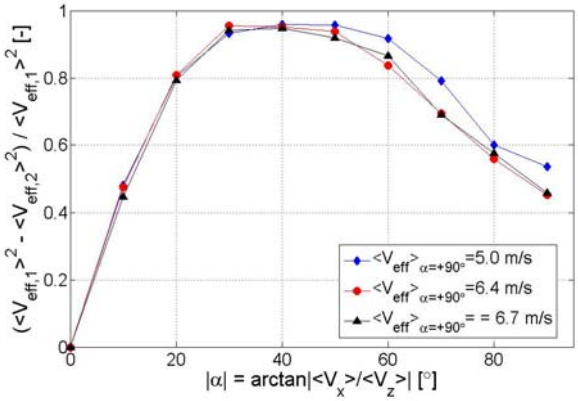

Figure 7. $\left(\langle V_{eff,1}\rangle^2 - \langle V_{eff,2}\rangle^2\right)/\langle V_{eff,1}\rangle^2$ versus $\arctan\left|\langle W_p\rangle/\langle V_p\rangle\right|$, measured for parallel probe angular calibrations. Suffix 1 and 2 indicate the non-blocking and blocking hot-film orientation, respectively.

Where for the angular calibration $\langle U_p\rangle = 0$ m/s, in the rotor wake generally $\langle U_p\rangle \neq 0$ m/s. For the present hot-film orientations, $U_p = U_m$, see Figure 6. As the $\langle U_m\rangle$-contribution to $\langle V_{eff}\rangle$ is symmetrical, $h^2\langle U_m\rangle^2$ is subtracted from each of the $\langle V_{eff}\rangle$-terms in equation [12], resulting in

$$\frac{\langle V_{eff,1}\rangle^2 - \langle V_{eff,2}\rangle^2}{\langle V_{eff,1}\rangle^2 - h^2\langle U_m\rangle^2} = G\left(\arctan\left|\frac{\langle V_m\rangle}{\langle W_m\rangle}\right|\right), \qquad [13]$$

written in global coordinates. Rewriting, using equation [9], yields

$$\frac{\langle V_{eff,1}\rangle^2 - \langle V_{eff,2}\rangle^2}{\langle V_m\rangle^2 + k^2\langle W_m\rangle^2} = G\left(\arctan\left|\frac{V_m}{W_m}\right|\right). \qquad [14]$$

$\langle W_m\rangle$ is determined using the traditional approach, leaving $\langle V_m\rangle$ the only unknown. The Newton-Raphson method solves for $|\langle V_m\rangle|$. Non-physical $\langle U_m\rangle^2$, $\langle V_m\rangle^2 < 0$ values are thus avoided. In the remainder of the discussion, the velocity components are expressed in global coordinate systems only, hence the subscript *m* is omitted from hereon.

3.3 Uncertainty Analysis For the traditional and the proposed method, an analysis into the uncertainty of the resulting average velocity vector $\langle\vec{V}\rangle(r, \theta, z, \theta_b)$ is performed. Both the velocity magnitude random uncertainty, $U_{|V|}$, and the flow angle random uncertainty, U_α, are studied. Bias uncertainties are not considered.
First, the contributions to $U_{|V|}$ are discussed.
Differences are found between $\overline{W}$, measured during speed calibration, and that computed from the speed calibration relation [4], using the corresponding $\overline{E}$-measurement. The uncertainty contribution $U_{|V|,sp.cal}$ is taken to be the normalized standard deviation over all data points,

$$U_{|V|,sp.cal.} = \left[\frac{1}{N}\sum_{i=1}^{N}\left(1 - \frac{\overline{W_m}}{\overline{W_c}}\right)^2\right]^{1/2}, \qquad [15]$$

with N the number of data points and $\overline{W_m}$, $\overline{W_c}$ the measured velocity and that computed from the speed calibration relation, respectively. Multiple measurements are needed to derive $\vec{V}$, using several speed calibration curves. Therefore, $U_{|V|,sp.cal}$ = 0.04, relative to $|\vec{V}|$, which is the maximum found with all speed calibrations, is used throughout.
The consistency in the speed calibration is studied by observing the differences between two successive speed calibrations of the same probe. Differences between successive speed calibration curves of the same probe yield an uncertainty contribution $U_{|V|,cons.}$, since both curves could be used to determine V_{eff}. To estimate $U_{|V|,cons}$, first $\overline{W}$ is computed for each calibration curve using a given series of $\overline{E}$ = 1.4, 1.5,…, 2.1 *V*. This $\overline{E}$-domain corresponds to a $\overline{W}$-range of approximately 0 to 9 m/s, the range expected for the present experiments. The velocity difference between successive calibrations is averaged over all $\overline{E}$-points, yielding $\overline{\overline{\Delta W}}$. The maximum for all pairs is found to be 0.3 m/s and correspondingly $U_{|V|,cons}$ = 0.3 m/s is selected.

The limited number of V_{eff}-samples, 54, per (r, θ, z, θ_b)-point introduces an uncertainty in the determination of the average, $U_{|V|,av.}$. The Student t probability distribution is used to compute the 99 % confidence limits of $\langle V_{eff}\rangle$ (Ref. 15), as it is assumed that the number of samples going to infinity, the distribution converges to a normal distribution. The confidence limits, normalised with $\langle V_{eff}\rangle$, are found for the wake passages are larger than for the remainder of the cycle, due to stronger velocity fluctuations in the wakes. Furthermore, $\langle V_{eff}\rangle$-confidence limits are larger near the blade root, r/R_t = 0.4, than at the mid-span and tip locations, r/R_t > 0.4, see Table 3. When assuming that $\langle V_{eff}\rangle \sim |\vec{V}|$, the values of Table 3 serve as conservative estimates of $U_{|V|,av.}$, relative to $|\vec{V}|$.

Table 3 Conservative estimates of the 99 % $\langle V_{eff}\rangle$ confidence limits, relative to local $\langle V_{eff}\rangle$

	r/R_t = 0.4	r/R_t > 0.4
Wake	0.10	0.05
Remainder	0.015	0.01

At each location, multiple measurements, with the hot-film in various orientations, are required to determine $\langle\vec{V}\rangle$. While Ψ and θ_{tip} can be kept constant, fluctuations in $Re_{0.7R}$, λ and $W_{jet\text{-}exit}$ occur. As the proposed data reduction approach requires six hot-film orientations, six $Re_{0.7R}$-, λ- and $W_{jet\text{-}exit}$-samples are available at each location. The 99 % confidence bounds for the average $Re_{0.7R}$ are determined at 3.5 %, hence the effect of $Re_{0.7R}$-fluctuations on the velocity is ignored.
The effects of fluctuations in λ and $W_{jet\text{-}exit}$ are quantified by considering the one-dimensional actuator disc axial momentum equation (Ref. 16)

$$c_T = 4a(1-a), \qquad [16]$$

with a the axial induction factor at the actuator disc. Recall that a is defined as (Ref. 16)

$$a = 1 - \frac{W}{W_\infty}, \qquad [17]$$

with W and W_∞ the axial velocity at the disc and the undisturbed axial velocity, respectively. c_T is not measured during hot-film traverses; linear interpolation between the measured (λ, c_T)-points for θ_{tip} = 2°, see Ref 11, is used instead to determine c_T for the λ found at each hot-film location, for each of the six measurements.
Per hot-film location, W/W_∞ can be computed both for each of the six measurements as well as $\overline{W}/\overline{W_\infty}$ for the average λ over the six measurements, using the estimated c_T and equations [16], [17].

Next, the ratio $W/\overline{W}$ is determined,

$$\frac{W}{\overline{W}} = \frac{W/W_\infty}{\overline{W}/\overline{W_\infty}} \cdot \frac{W_\infty}{\overline{W_\infty}}, \qquad [18]$$

using the assumption that $W_\infty = W_{jet\text{-}exit}$. The 99 % confidence bounds for the average of the six $W/\overline{W}$-samples per hot-film location are determined with the Student t probability distribution. Across all hot-film locations, a conservative estimate for the 99 % confidence bounds is 0.03. With the assumption that $\overline{W} \sim |\vec{V}|$, we define $U_{|V|,cond.} = 0.03$, relative to $|\vec{V}|$.

Due to small, random drifts in the traversing mechanism, the hot-film (r, θ) -location cannot be reproduced exactly for the set of required measurements. As a conservative estimate, the location uncertainty is set to ± 0.01 m in the (y_m, z_m) –coordinates for each hot-film location. The uncertainty can be translated into cylindrical (r_m, θ) -coordinates.

For given θ, $|\vec{V}|$ is averaged over θ_b per radial location. Linear interpolation between the radial locations suggests that the present r-location uncertainty does not induce a significant $|\vec{V}|$-uncertainty and is thus neglected.

The θ-location uncertainty ranges from 2.5° at r/R_t = 0.4 to 1.0° at r/R_t = 1. It effectively causes a θ_b-uncertainty of identical magnitude.

The θ_b-uncertainty results in a $|\vec{V}|$-uncertainty for given θ_b. Every 2° θ_b a V_{eff}-recording is taken, an acceptable uncertainty interval thus is

$$U_{|V|,loc.}(\theta_b) = \max\left(\left|\left|\vec{V}\right|(\theta_b) - \left|\vec{V}\right|(\theta_b + 2^\circ)\right|, \ldots \left|\left|\vec{V}\right|(\theta_b) - \left|\vec{V}\right|(\theta_b - 2^\circ)\right|\right) \qquad [19]$$

All uncertainty contributions are assumed independent and are thus added orthogonally,

$$U^2_{|V|} = U^2_{|V|,sp.cal.} + U^2_{|V|,cons.} + U^2_{|V|,av.} + \ldots U^2_{|V|,cond.} + U^2_{|V|,loc.}. \qquad [20]$$

For all (r, θ, z)-locations, $U_{|V|}$ can be computed as a function of θ_b, see Figures 8 and 9. Generally, the order of magnitude of $U_{|V|}$, relative to |<V>|, is 10 %. The large uncertainty levels in the vicinity of the blade passage are due to the large $d|\langle\vec{V}\rangle|/d\theta b$-gradients and correspondingly large $U_{|V|,loc.}$.

For U_α a similar analysis is made. Contributions due to non-constant angular calibration constants, $U_{\alpha,\ ang.cal}$, and due to inconsistency between successive angular calibrations, $U_{\alpha,cons.}$ are identified.

The angular calibration constants are derived with equations of the type [6]. Discrepancies are found however when comparing angular calibration data and equations of the type [6];

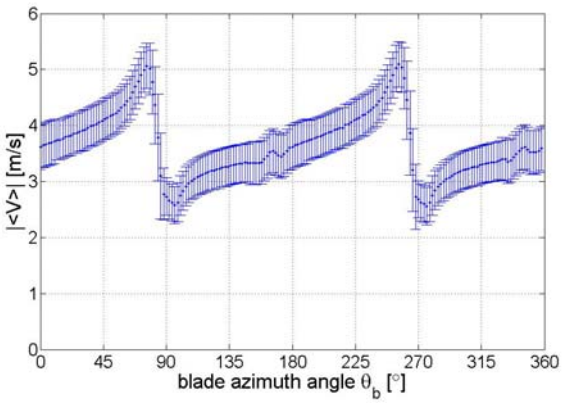

Figure 8. $|\langle\vec{V}\rangle|$ versus θ_b, including the total random uncertainty interval, for (r, θ, z) = (0.42 m, 270°, 0.06 m). Blade passage: $\theta_b \approx$ 90°, 270°, wake passage: $\theta_b \approx$ 180°, 360°.

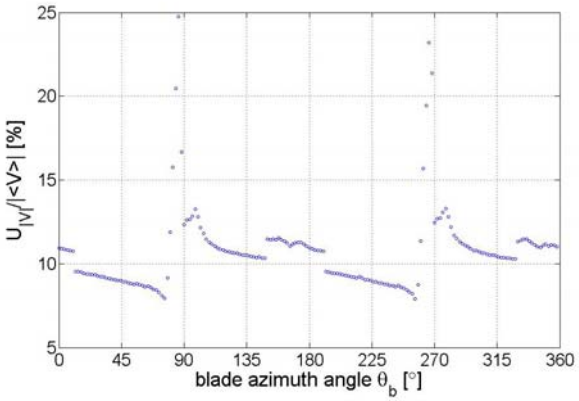

Figure 9. Total random uncertainty interval, relative to $|\langle\vec{V}\rangle|$, versus θ_b, for (r, θ, z) = (0.42 m, 270°, 0.06 m). Blade passage: $\theta_b \approx$ 90°, 270°, wake passage: $\theta_b \approx$ 180°, 360°.

α_c computed with equations of the type [6] for measured values of $\overline{V_{eff}}/\left|\overline{\vec{V}}\right|$ does not coincide with α_m at which the calibration is taken. For each angular calibration, the standard deviation is determined and taken as the uncertainty contribution,

$$U_{\alpha,ang.cal.} = \left[\frac{1}{N}\sum_{i=1}^{N}(\alpha_c - \alpha_m)^2\right]^{1/2}, \qquad [21]$$

with N =19 samples per calibration, α = -90˚, -80˚,…,90˚. The maximum value for all angular calibrations is found to be 4˚, hence as a conservative estimate, $U_{\alpha,ang.cal.}$ = 4˚ is used throughout.

As noted in § 3.1, the calibration constants can be considered independent of $|\vec{V}|$. The consistency of successive angular calibrations is studied, since a measurement could use the angular calibration constants from either the

preceding or the succeeding angular calibration. A range of $\overline{V_{eff}} / \left|\overrightarrow{V}\right|$-values is selected that approximately covers α = [0˚, 90˚] in i.e. equation [6]. For each $\overline{V_{eff}} / \left|\overrightarrow{V}\right|$-value, the corresponding α is computed and the average difference $\left|\overline{\Delta\alpha}\right|$ between successive angular calibrations is determined. The maximum for all pairs is found to be 3˚ and correspondingly $U_{\alpha,cons.}$ = 3˚.

The two U_α-contributions are independent and can thus be added orthogonally,

$$U_\alpha^2 = U_{\alpha,ang.cal.}^2 + U_{\alpha,cons.}^2, \quad [22]$$

resulting in U_α = 5˚ that is used throughout the measurement campaign.

The uncertainty in the derivation of c_T is discussed in detail in Ref. 12. The maximum random uncertainty interval is given by $U_{cT} = 1.8 \cdot 10^{-2}$.

4 Results

4.1 Comparison with Published Results As a first step, present results are compared with published hot-wire anemometry results, measured 6.0 cm downstream of the same rotor, in the same wind tunnel, under the same conditions; Ψ = 0˚, θ_{tip} = 2˚, λ = 8 and $W_{jet\text{-}exit}$ = 5.5 m/s (Ref. 4, 5). The published data is derived with the traditional data reduction approach. Whereas 54 V_{eff}-samples per θ_b are used with the present measurements to determine $\langle V_{eff}\rangle$, 10 samples are used with the published measurements. In Ref. 4, 5 the V_{eff}-recordings with the wire in the axial direction are done with a normal probe instead of a, more suited, parallel probe.

Individual comparisons of the cylindrical velocity components $\langle V_r\rangle$, $\langle V_\theta\rangle$, $\langle V_z\rangle$ are made. For $\langle V_z\rangle$, the agreement is good, see Figure 10 as an example. The difference between previously published and present data is significantly smaller than the uncertainty bounds of the present data set. For this hot-film position, maximum and average absolute $\langle V_z\rangle$-differences are 0.3 m/s and 0.1 m/s, respectively. The larger number of samples for the present measurements causes the that $\langle V_z\rangle(\theta_b)$-distribution to be smoother. The good agreement increases confidence in the present data.

The comparisons of <Vr> and <Vθ> are extended to include the traditional data reduction approach applied to the present measurements. The effect of the unequal sample number on the comparison between

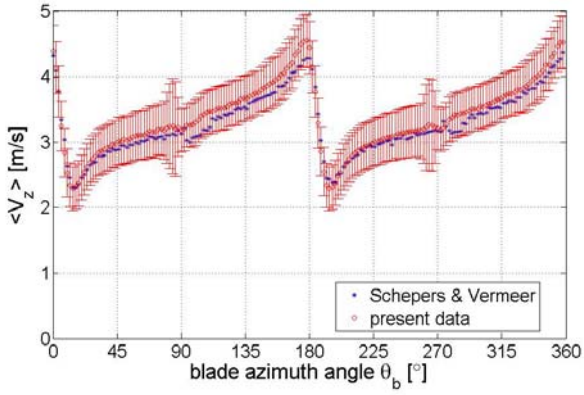

Figure 10. $\langle V_z\rangle$ versus θ_b at (r, θ, z) = (0.42 m, 180°, 0.06 m) for Schepers and Vermeer [ref] and present data. For the present data, uncertainty bounds are included. Blade passage: $\theta_b \approx$ 0°, 180°, wake passage: $\theta_b \approx$ 90°, 270°.

the traditional and the proposed data reduction is hence eliminated.

The orders of magnitude of $\langle V_r\rangle$ and $\langle V_\theta\rangle$ are comparable for all three data sets, see e.g. Figures 11 and 12.

For $\langle V_r\rangle$, the proposed approach yields a less wiggly result than both traditional approach data sets. The $\langle V_r\rangle$-wiggles thus appear to be a characteristic of the traditional approach. Furthermore, the proposed approach yields clear responses to blade and wake passages.

Whereas $\langle V_r\rangle$ is positive throughout the cycle for (r, θ, z) = (0.42 m, 180°, 0.06 m), corresponding to wake expansion, $\langle V_\theta\rangle$ apparently changes sign, see Figure 12.

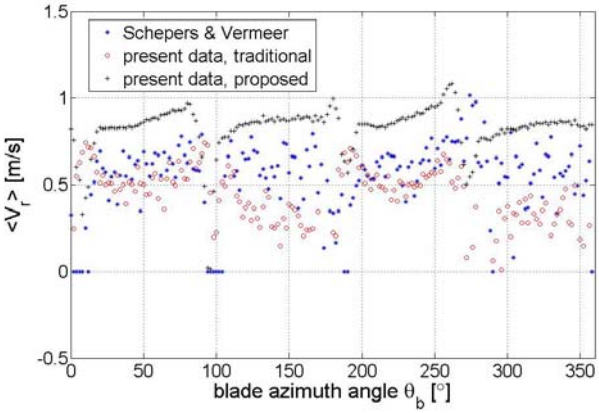

Figure 11. $\langle V_r\rangle$ versus θ_b at (r, θ, z) = (0.42 m, 180°, 0.06 m) for Schepers and Vermeer [ref] and present data. Both the traditional and the proposed approach are used with the present data. Blade passage: $\theta_b \approx$ 0°, 180°, wake passage: $\theta_b \approx$ 90°, 270°.

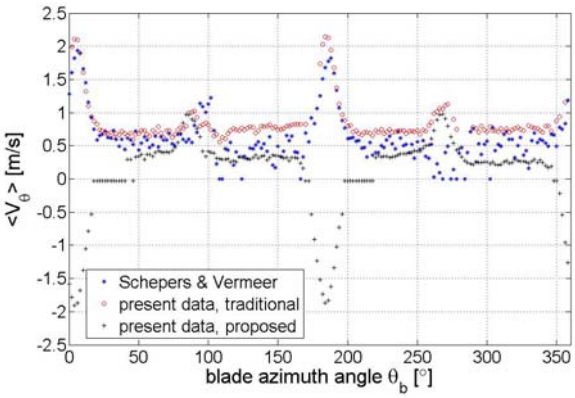

Figure 12. $\langle V_\theta \rangle$ versus θ_b at (r, θ, z) = (0.42 m, 180°, 0.06 m) for Schepers and Vermeer [ref] and present data. Both the traditional and the proposed approach are used with the present data. Blade passage: $\theta_b \approx 0°$, 180°, wake passage: $\theta_b \approx 90°$, 270°.

The change in $\langle V_\theta \rangle$-direction is apparent since the proposed approach yields the direction of the velocity components as part of the solution. The traditional approach cannot give velocity component directions. A comparison of the two traditional approach $\langle V_\theta \rangle$-data sets learns that the increased number of samples reduces the wiggles in the data.
A comparison with Ref. 6 is performed. Its rotor, operating conditions and wind tunnel are different than used with the current measurements. The X-probe technique in Ref. 6 yields the directions of the velocity components. Qualitative agreement in $\langle V_z \rangle$ and $\langle V_\theta \rangle$ is found. The sign change in $\langle V_\theta \rangle$ is present in both data sets. These observations increase confidence in the present data.
It is concluded that the proposed approach reveals more detail in the $\langle V_r \rangle$- and $\langle V_\theta \rangle$-distribution than the traditional approach. The remainder of the discussion is therefore based upon velocity determined with the proposed approach.

4.2 Axial Induction Factor An analysis of the axial induction factor a in the rotor plane, defined in equation [17], is conducted. Measurements cannot be performed in the rotor plane itself using hot-wires, hence a has to be estimated using the measured axial velocity in the planes 6.0 cm upstream and 3.5, 6.0 and 9.0 cm downstream of the rotor plane.
For each (r, θ, z)-location, $\langle V_z \rangle$ is first averaged over θ_b. Next, a "local" a is determined at each location, using equation [17], with W_∞ the average over the three $W_{jet\text{-}exit}$-values that go with the hot-film measurements required to determine $\langle V_z \rangle$. Per (r, θ)-position, the a-data at the four z-locations is used to define a linear function in the Least Square sense. The linear function is used to find a at z = 0 cm, the rotor plane, see Figure 12.
A radial dependency of a can be observed. The axisymmetry in a is distorted by the nonuniformity of the empty jet, see § 2.2. In order to reduce the nonuniform flow effects, data from θ-locations that are positioned in areas where a is strongly non-axisymmetrical should be omitted. The remaining θ-range, given by θ = [30°, 135°] U [225°, 315°], is named θ^*.

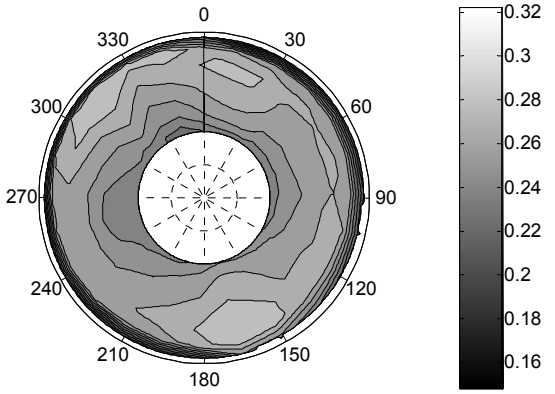

Figure 12. contours of induction factor a at the rotor plane, computed from linear Least Squares fit of the data at 6.0 cm upstream and 3.5, 6.0 and 9.0 cm downstream.

When only considering the θ^*-range, the r-dependency of a is confirmed, see Figure 13. Actuator disc theory on the contrary uses the assumption of a constant a (Ref. 16). The finite number of blades causes a to approach 0 near the blade tip, since a reaches 0 at some distance outboard of the wake in a continuous fashion. For r/R_t = 1, significant a-variations with θ can be found, see the standard deviation signal in Figure 13. The effects of empty jet non-uniformity and drifts in the hot-film positioning on the measured data are

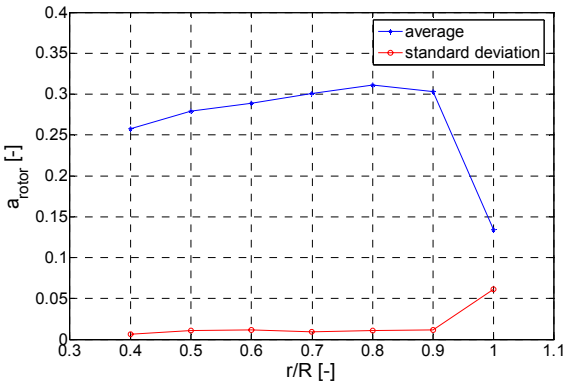

Figure 13. Average and standard deviation of the axial induction factor $a(r)$, determined using the samples in the θ^*-range, for a given r.

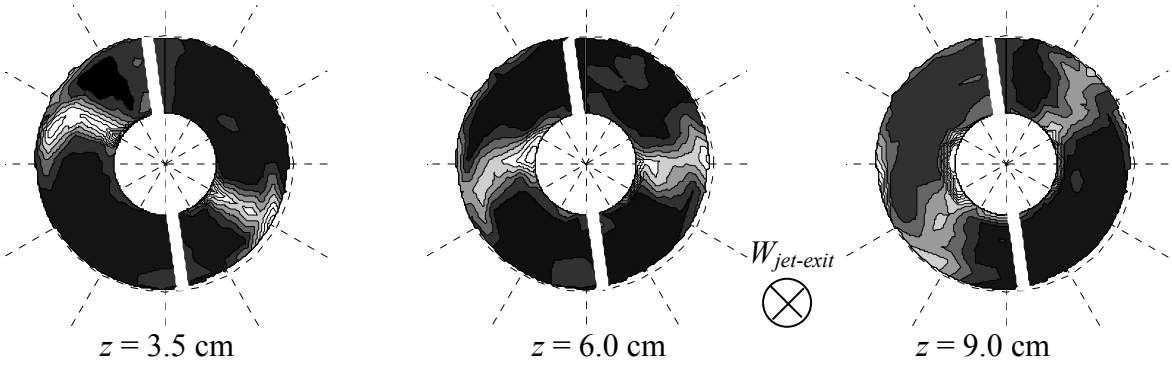

Figure 14. Contour plots of standard deviation $s_{Veff}(r, \theta, z, \theta_b)$ at θ_b = 172°, at downstream planes z = 3.5, 6.0 and 9.0 cm, for Ψ = 0°. The two blades, indicated in white, rotate clockwise. $\overrightarrow{W_{jet-exit}}$ is directed away from the observer. Going downstream, the wake diffuses and the relatively straight shape, observed at z = 3.5 cm, deforms.

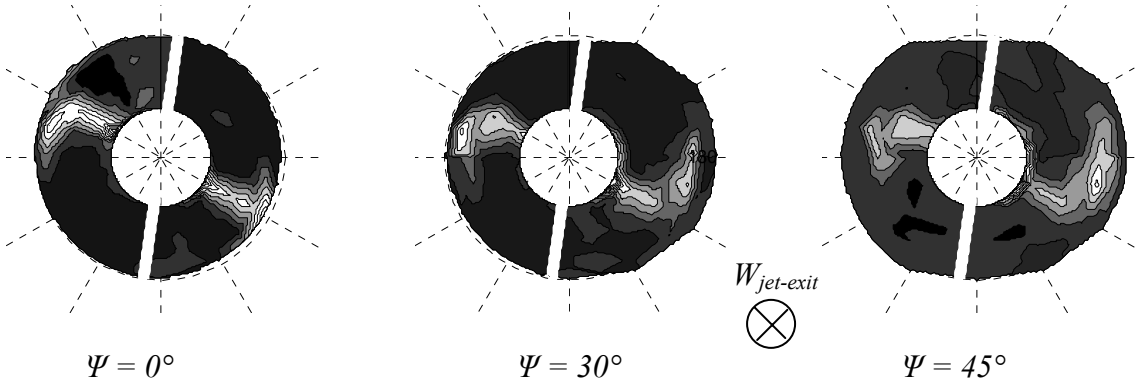

Figure 15. Contour plots of standard deviation $s(r, \theta, z, \theta_b)$ at θ_b = 172°, at yaw angles Ψ = 0°, 30° and 45°, for z = 3.5 cm. The two blades, indicated in white, rotate clockwise. $\overrightarrow{W_{jet-exit}}$ is directed away from the observer and, for $\Psi \neq 0°$, to the right. With larger Ψ, the asymmetry in the wake is increased.

magnified by the proximity of the concentrated tip vortices for the hot-film position r/R_t = 1.

Using axial momentum theory, the local a in the rotor plane can be correlated to a local thrust coefficient c_T, equation [16]. Discrete integration over the rotor plane, using the assumption that c_T = 0 at the blade root R_r, yields, for the rotor, C_T = 0.77 at λ = 8, θ_{tip} = 2°, Ψ = 0°. When only using the θ^*-range, we find C_T^* = 0.76. A ± 10 % uncertainty bound on W/W_∞ appears reasonable from § 3.3. Consequently, an uncertainty bound of -0.16, +0.12 is found for C_T.

Axial force is also measured using calibrated strain gauges placed on the rotor shaft (Ref. 12). For λ = 8, θ_{tip} = 2°, Ψ = 0° we find C_T = 0.87 ± 0.02. Hence, although a substantial difference of 0.1 between C_T from force measurements and from axial momentum theory is observed, the difference is of the order of magnitude of the uncertainty bounds. A physical ground for the difference can also be identified; the momentum approach is based upon actuator disc theory, applied locally. Instead of an actuator disc with an infinite number of blades, in reality only two blades are present. The approach of averaging $\langle V_z \rangle$ over θ_b to arrive at a seems too simple to represent the more complex reality.

4.3 Understanding the Velocity Signals The first observation that can be made is that the standard deviation of V_{eff}, determined over 54 samples per (r, θ, z, θ_b), is an effective tool to find the wake passage. For all six hot-film orientations used to determine the velocity vector, a coinciding local s_{Veff}-increase is found for the θ_b-range where a wake passage is expected. This can be explained by the turbulence in the wake, yielding larger disturbances than outside of the wake. As shown in Figures 14 and 15 for the normal

probe with the hot-film vertically, qualitative observations on wake convection and wake shape can be made from s_{Veff}. The wake diffuses and deforms while being convected downstream, see Figure 14. Furthermore, yawed flow conditions induce wake asymmetries, see Figure 15.

For the $<V_{eff}>$-discussion, a typical mid span location of (r, θ) = (0.36 m, 270°) is selected for axial flow conditions, not to complicate matters. All three downstream planes, at z = 3.5, 6.0 and 9.0 cm, are considered. The observed trends in velocity signals can be explained by considering a typical wake vortex model, see Figure 16. For the mid span location, the response to the blade passage is dominated by bound vorticity at the blade, the response to the wake passage by the vorticity trailed in the wake.

The sign of the bound vortex, positive outboard, corresponds to the observed $<V_z>$-trend at the blade passage; a maximum followed by a minimum, see Figure 17.

The $<V_\theta>$-minimum at the blade passage, see Figure 18, also agrees with the bound vortex sign. Near the blade passage, the flow thus rotates in the direction opposite to the blade rotation. The observation agrees with the conservation of angular momentum; the flow downstream of the rotor should rotate in the direction opposite to the rotor, in reaction to the torque applied by the flow on the rotor. With increased downstream hot-film position, the amplitude of the $<V_z>$- and $<V_\theta>$-responses to blade passages reduces, as expected.

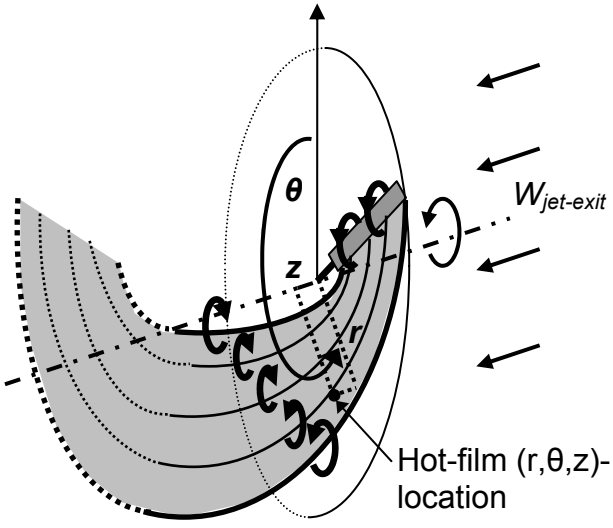

Figure 16. Typical wake vortex model. Direction of bound and trailed circulation is indicated. The location of a hot-film probe is included.

In general, positive values for $<V_r>$ are found, with the sign convention of $V_r > 0$ in the outboard direction: the wake is expanding, as expected. The radial velocity is also affected by a blade passage, see Figure 19. The general $<V_r>$-increase over a blade passage, seen for all z-locations in Figure 19, can be explained by the presence of the bound vorticity and the observation that the blade is rotating, not translating. When approaching the hot-film location, the bound vortex on the blade will induce a radially inboard velocity component. The induced $<V_r>$-component is in the outboard direction when the blade moves away from the hot-film location. The change of $<V_r>$-sign causes the $<V_r>$-increase over a blade passage. Although the general $<V_r>$-increase with a blade passage can clearly be observed for all three z-locations in Figure 19, the details are not consistent for the three measurements.

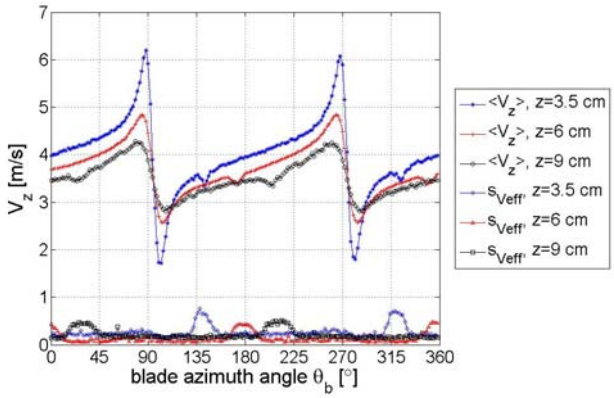

Figure 17. $<V_z>$ and s_{Veff} versus θ_b for z = 3.5, 6.0 and 9.0 cm downstream, for (r, θ) = (0.36 m, 270°). Blade passage: $\theta_b \approx$ 90°, 270°, wake passage: at local s_{Veff}-increase.

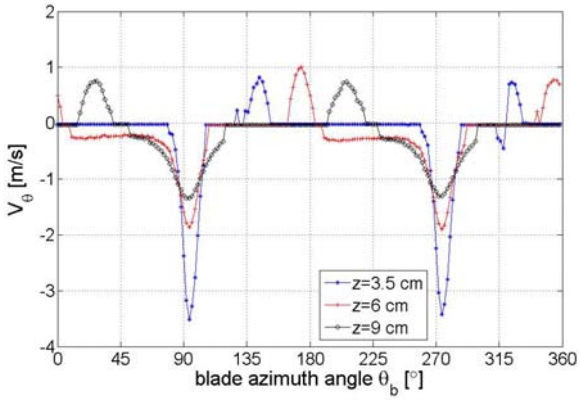

Figure 18. $<V_\theta>$ versus θ_b for z = 3.5, 6.0 and 9.0 cm downstream, for (r, θ) = (0.36 m, 270°). Blade passage: $\theta_b \approx$ 90°, 270°, wake passage: at local s_{Veff}-increase in Figure 17.

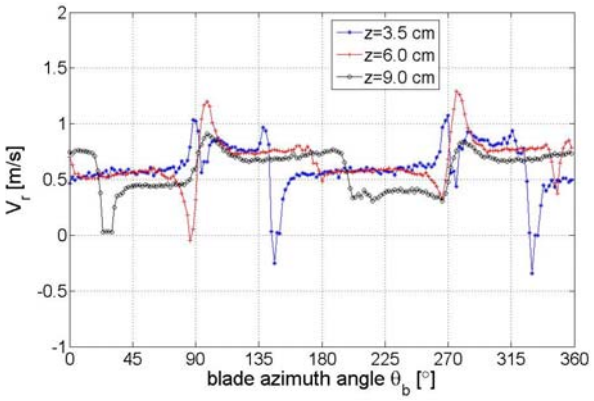

Figure 19. <V_r> versus θ_b for z = 3.5, 6.0 and 9.0 cm downstream, for (r, θ) = (0.36 m, 270°). Blade passage: $\theta_b \approx 90°, 270°$, wake passage: at local s_{Veff} -increase in Figure 17.

Using the inviscid wake vortex model, only the <V_r>-response to a wake passage can be explained. <V_r> induced by trailed vorticity changes sign with a wake passage. The sign change causes the <V_r>-jump, see Figures 19 and 20. The sign of the trailed vorticity depends on the *r*-location where it trails the blade, due to the circulation distribution on the blade itself. The sign of the <V_r>-jump thus is dependent on the *r*-location in the wake.

This phenomenon is observed in the measurements, compare Figures 19 (r/R_t = 0.6) and 20 (r/R_t = 0.9); for all *z*-locations, the signs of the <V_r>-jumps are opposite and agree with the wake vortex model.

The local <V_z>-minimum and <V_θ>-maximum at a wake passage, see Figures 17 and 18, are associated with viscous effects in the wake.

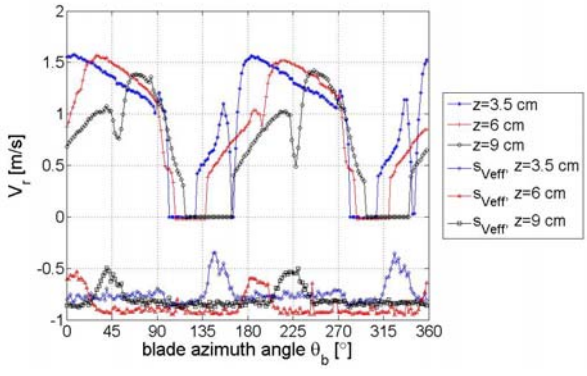

Figure 20. <V_r> and s_{Veff}, offset by -1 m/s, versus θ_b for z = 3.5, 6.0 and 9.0 cm downstream, for (r, θ) = (0.54 m, 270°). Blade passage: $\theta_b \approx 90°, 270°$, wake passage: at local s_{Veff}-increase. Note the <V_r>-increase across the wake passage.

Both velocity responses display the drag, loss of momentum, in the wake. The local <V_z>-minimum represents the axial momentum loss of the flow, hence the contribution to the axial force on the rotor due to viscous drag. The local <V_θ>-maximum represents a reduction in angular momentum of the flow, corresponding to a reduced net torque applied to the rotor.

Conclusions

Single film hot-film measurements in the near wake behind a 0.6 m radius rotor model placed in an open jet wind tunnel are performed. Three downstream (3.5, 6.0 and 9.0 cm) and one upstream plane (6.0 cm), all parallel to the rotor plane, are selected. The hot-films make traverses through these planes. With an undisturbed wind speed $W_{jet\text{-}exit}$ 5.5 m/s, the tip speed ratio λ is set to 8. The yaw angle Ψ is set to either 0˚, 30˚ or 45˚.

The three velocity components are determined as a function of the blade azimuth angle θ_b. The traditional velocity determination approach cannot predict the direction of velocity components. The radial and tangential velocity components that are small compared to the axial velocity component, are poorly predicted; the results are wiggly and squared velocity components smaller than zero, hence unphysical, occur.

A new velocity determination approach that should overcome these deficiencies is proposed. It is shown that this technique is capable of predicting the direction of the radial and tangential velocity components as well as giving a consistent estimate of their magnitudes. Hence the proposed velocity determination approach is preferred over the traditional one.

A detailed analysis into both the velocity magnitude uncertainty $U_{|V|}$ and flow angle uncertainties U_α of the θ_b-dependent velocities is conducted. It is concluded that generally, the order of magnitude of $U_{|V|}$, relative to $|\vec{V}|$, is 10 % and that U_α = 5˚.

Published hot-wire data on the same rotor under the same operating conditions in axial flow is used for comparison. The differences between the two data sets in the axial velocity component are significantly smaller than the uncertainty bounds, thereby increasing confidence in the present data. As the published data uses the traditional velocity determination approach, the radial and tangential velocity component comparisons clearly demonstrate the advantages of the proposed approach: the direction of the radial and tangential velocity components is predicted, whilst estimated magnitudes are consistent.

The standard deviation in the θ_b-dependent measured effective velocity signal can be used to locate the wake. Wake deformation and, for yawed flow conditions, wake asymmetry are observed.
The trends in all three velocity components with blade and wake passages agree with those expected from a vortex wake model, where the viscosity is confined to the vortex sheet. The agreement increases confidence in the present data set.

References

[1] Leishman, J.G., Challenges in modelling the unsteady aerodynamics of wind turbines, Wind Energy, Vol. 5, April-September 2002, pp. 85 – 132.

[2] Snel, H., Review of the Present Status of Rotor Aerodynamics, Wind Energy, Vol. 1, April 1998, pp. 46-69.

[3] Vermeer, L.J., Sørensen, J.N. and Crespo, A., Wind turbine wake aerodynamics, Progress in Aerospace Sciences, Vol. 39/6-7, August-October 2003, pp. 467-510.

[4] Vermeer, L.J., Wind Tunnel Experiments on a Rotor Model in Yaw, Proceedings of the 12th IEA Symposium on the Aerodynamics of Wind Turbines, B.M. Pedersen, eds., IEA, Lyngby, Denmark, 1998, pp. 11-20.

[5] Schepers, J.G., An Engineering Model for Yawed Conditions, Developed on Basis of Wind Tunnel Measurements, AIAA-1999-0039, 18th ASME Wind Energy Symposium, 37th Aerospace Sciences Meeting and Exhibit, ASME, Reno, NV, 1999.

[6] Ebert, P.R. and Wood, D.H., The Near Wake of a Model Horizontal-Axis Wind Turbine-I. Experimental Arrangements and Initial Results, Renewable Energy, Vol. 12, 3, 1997, pp. 225 – 243.

[7] Ebert, P.R. and Wood, D.H., The Near Wake of a Model Horizontal-Axis Wind Turbine-II. General Features of the Three-Dimensional Flowfield, Renewable Energy, Vol. 18, 1999, pp. 513 – 534.

[8] Ebert, P.R. and Wood, D.H., The Near Wake of a Model Horizontal-Axis Wind Turbine Part 3: Properties of the Tip and Hub Vortices, Renewable Energy, Vol. 22, 2001, pp. 461 – 472.

[9] Whale, J., Anderson, C.G., Bareiss, R. and Wagner, S., An Experimental and Numerical Study of the Vortex Structure in the Wake of a Wind Turbine, J. Wind Eng Ind Aerodyn, Vol. 84, 2000, pp. 1 – 21.

[10] Grant, I. and Parkin, P., A DPIV Study of the Trailing Vortex Elements from the Blades of a Horizontal Axis Wind Turbine in Yaw, Experiments in Fluids, Vol. 28, 4, April 2000, pp. 368 – 376.

[11] Vermeer, L.J., A Review of Wind Turbine Wake Research at TUDelft, AIAA-2001-0030, 20th ASME Wind Energy Symposium, 39th Aerospace Sciences Meeting and Exhibit, ASME, Reno, NV, 2001.

[12] Haans, W., Sant, T., Van Kuik, G.A.M. and Van Bussel, G.J.W., Measurement and Modelling of Tip Vortex Paths in the Wake of a HAWT under Yawed Flow Conditions, AIAA-2005-0590, 24th ASME Wind Energy Symposium, 43rd AIAA Aerospace Sciences Meeting and Exhibit, Reno, NV, 2005, pp. 136-145.

[13] Mast, E.H.M., Estimating the Circulation Distribution using Near Wake Velocity Measurements, Master thesis WE-03190, Section Wind Energy, Delft University of Technology, Delft, The Netherlands, 2003.

[14] Bruun, H. H., Hot-Wire Anemometry, Oxford Science Publications, Oxford, England, 1995.

[15] Barlow, J.B., Rae, W.H. Jr. and Pope, A., Low Speed Wind Tunnel Testing, 3rd edition, Wiley Interscience, New York, United States, 1999.

[16] Burton, T., Sharpe, D., Jenkins, N. and Bossanyi, E., Wind Energy Handbook, Wiley, Chichester, England, 2001.